17

ENTANGLED GRANULAR MEDIA

NICK GRAVISH & DANIEL I. GOLDMAN

School of Physics, Georgia Institute of Technology, Atlanta, GA, USA

Granular materials (GM) are collections of discrete, dissipative, and athermal particles [1–4] and when dry, GM interact through frictional and repulsive forces only. GM are important in industry, engineering, and science, in daily life are commonly encountered as bags of coffee, rice, sugar, etc. Despite the apparent simplicity of particle–particle interaction in dry GM, collections of even simple spherical particles may exhibit complex rheological properties such as transitioning between jammed and flowing states (see Ref. 5 for a comprehensive overview). Study of GM is motivated by industrial and engineering applications in addition to fundamental science research. Experiments on GM often use simple table-top apparatus' in which the forces and motion can be visualized with visible light cameras, thus making GM research very accessible. Lastly, GM can be simulated using the discrete element method (DEM), which enables tandem computational and experimental studies of GM [6–11].

The study of how soft matter flows under external or internal stresses is called rheology [1–4]. The development of principles of granular rheology is a focus of GM research. One area of granular rheology study is to understand how the features of the granular particle—such as roughness, shape, or material stiffness—may influence the material properties (e.g., stiffness or yield strength) of the bulk GM. The majority of such rheological studies have focused on particles of convex shape [2, 12–14], and less research has been focused on concave particles [15–17]. However, recent studies have shown that nonconvex particles display rheological properties that may be desirable for engineered GM, such as nonzero tensile strength, high
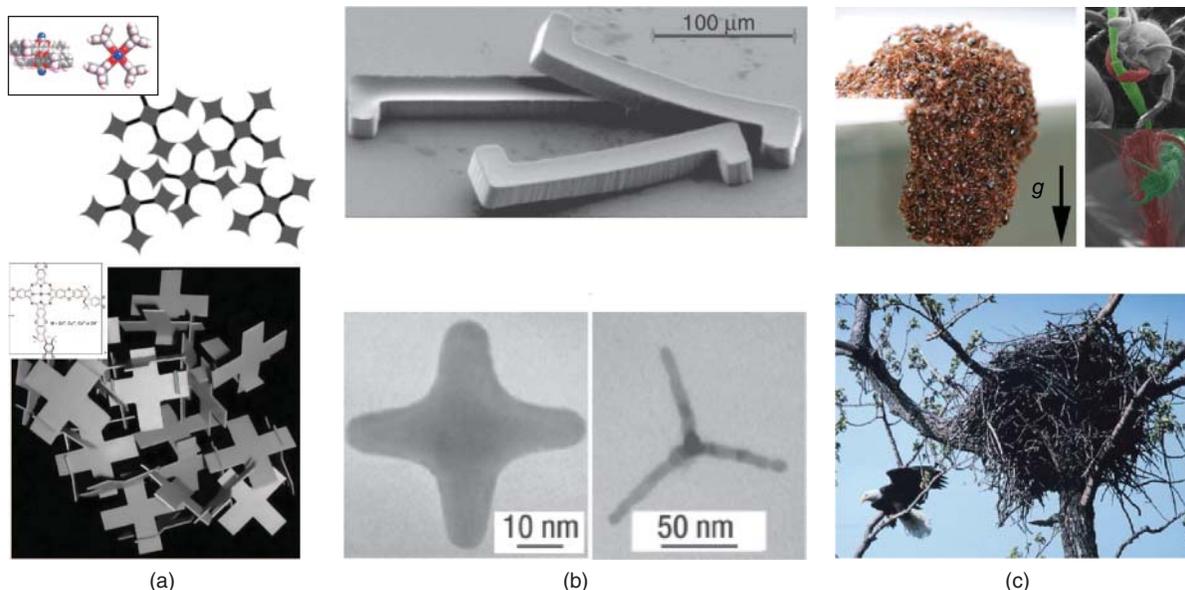
Figure 17.1 Concave particle assemblies from the nanoscale to macroscale. (a) Macromolecular assemblies of rigid oligomers (insets) interpenetrate depending on oligomer shape (top); Source: McKeown and Budd [24] and may form into large entangled networks (bottom); Source: McKeown *et al.* [25]. Particle dimensions are in the nanometer scale. (b) Concave particle suspensions (top); Source: Brown *et al.* [17] and concave colloids (bottom-left); Source: Manna *et al.* [22] and (bottom-right); Chen *et al.* [32]. (c) Concave particle assemblies found in nature, living fire ants (top), and rigid branches of bald eagles nests (bottom). Source: Mlot *et al.* [28].

yield stress, and desirable compaction properties [18, 19]. Thus, a new focus on nonconvex GM will impact scientific and engineering pursuits as diverse as jamming and soft robotics [20], designed granular materials [19], industrial granular processes, and a better understanding of soft matter systems [21].

Examples of nonconvex particle assemblies can be found at all scales of natural and industrial systems (Fig. 17.1). While few nonconvex granular materials studies have been performed, nonconvex particles are currently a focus of engineering efforts at the microscale and nanoscale [22, 23]. For example, macromolecules with concave shapes pack together with large voids in the bulk, which results in materials with a high microporosity [24, 25] (Fig. 17.1). Such high microporosity materials have applications ranging from nanodrug delivery systems to gas trapping [24, 25]. Furthermore, the design of concave colloidal particles have application to self-organizing, smart materials [26]. In addition to engineered systems, concave particles are found in biological systems (Fig. 17.1). The packing of actin or other protein filaments within eukaryotic cells has been modeled as concave granular materials [27]. The bridges and rafts collectively built by ants [28–30] are held together through the entanglement of ant limbs and mandibles, which can be considered concave particles. Structures constructed by animals from branches and twigs such as birds' nests may be considered as concave granular materials [31].

The goal of this chapter is to understand how the shape of a simple nonconvex particle - a "u-particle" influences bulk rheology. In experiment and computer simulation, we systematically study how particle concavity affects bulk properties of a granular material. The fundamental difference between concave and convex particle assemblies is the ability for concave particles to interpenetrate, which we call being entangled. Mechanical entanglement of particles alters the rheology of particle assemblies through their resistance to separate. In Section 17.1, we review previous studies of convex granular materials. Additionally, we introduce experimental techniques used to characterize granular rheology. In Section 17.2, we describe our experiments studying the stability of assemblies of U-shaped concave particles in which we vary concavity. In Section 17.3, we describe theoretical and numerical modeling of u-particle assemblies and their implications for assembly stability. In Section 17.4, we discuss the implications for these results to other systems of concave particles.

17.1 GRANULAR MATERIALS

17.1.1 Dry, Convex Particles

Granular materials are assemblies of macroscopic particles that are typically of size greater than $10\,\mu m$ [33]. Particles smaller than $10\,\mu m$ are subject to thermal effects while

granular materials are athermal [33]. Granular materials come in many shapes and sizes [14]; however, in the majority of physics studies granular materials are convex (often spherical) particles.

A simple experiment with GM is to pour particles of a known density and mass into a container and measure the volume occupied by the assembly. This experiment measures the fraction of total volume, V, versus the solid particle volume, V_p, and is called the volume fraction $\phi = \frac{V_p}{V}$. Mechanically stable ensembles of spherical, dry granular materials are found in a range of ϕ from random loose-pack $\phi_{rlp} \approx 0.55$ [4, 34] to random close-pack volume fraction $\phi_{rcp} \approx 0.64$ [4]. The maximum ϕ for ordered, uniform, spheres is that of a face-centered-cubic lattice in which $\phi_{fcc} = 0.77$. A loose, ordered, packing is that of a simple-square lattice with $\phi_{ssl} = 0.52$. Although the packing fraction of ordered ensembles (i.e., on a lattice) may be analytically solved for, the calculation of the maximum ϕ of randomly distributed particles of arbitrary shape must be done computationally [13].

A fundamental feature of granular materials is their ability to act like solids, fluids, or gases [2]. The "phase" of the granular material may spontaneously change under an applied load or other perturbation. An avalanche down a granular slope is an example of such a transition: the slope begins as an inert solid until an external perturbation is applied (tilting the slope for instance) after which a section of the slope becomes unstable, and the grains are put into motion. Avalanches typically occur above immobile grains trapped below, an example of the coexistence between the fluid-like and solid-like states of GM.

Dry granular materials consist of particles that interact through frictional and repulsive forces only [1–4]. Forces within a granular material are spatially heterogeneous and are transmitted through filamentary force chains [35, 36]. Because of the absence of particle–particle attraction, dry, spherical granular material cannot support tensile loading [3]. Furthermore, since particle–particle interactions are frictional, the force laws of granular flows are typically rate insensitive at low speeds [3]. At higher flow speeds, however, momentum transfer between particles becomes important and force laws take on a velocity dependence (with a force law dependent on the packing density of the material [37]).

17.1.2 Cohesion through Fluids

When water is added to a granular material, particles can cohere through the formation of capillary bridges (see Refs 38, 39 for comprehensive reviews). Unlike dry GM, wet granular media can support tensile loading because of the particle–particle attraction from capillary bridges [40, 41]. The attractive force from a capillary bridge between two wettable granular spheres is proportional to the surface tension of the fluid and inversely proportional to the radius

of curvature. Thus, the strength of the capillary bonds and the rheology of the bulk in general are sensitive to the fluid chemistry, the particle diameter, and the fluid volume.

The presence of even a small amount of water can dramatically alter the rheology of a granular material. In a dry granular material, the maximum slope angle that can be formed is $\approx 30°$. However, wet GM can be formed into piles and structures with much steeper slopes of $90°$ or above [42, 43]. It is because of this property that sandcastles are able to be built and structurally supported. The angle of repose of a wet GM is a function of the fraction of water present [43] and is a useful metric for determining the cohesion between grains.

Another technique for characterizing the strength of capillary bonds in a wet GM is to study the solid to fluid transition of the ensemble under vertical vibration [44, 45]. When the GM is in the fluid state, capillary bonds are repeatedly broken and reformed. The parameters of the fluid–solid transition for a given granular material are thus related to the strength of the capillary bonds between grains. It has been shown that the vibration energy (peak kinetic energy for sinusoidal vibrations) at which the fluid–solid transition occurs in wet granular materials is linearly proportional to the capillary bond energy [46]. Thus, vibration and relaxation experiments give insight into the particle–particle interactions in wet GM, and we look to these techniques for inspiration in the work we describe next.

17.1.3 Cohesion through Shape

Addition of fluid to dry granular media is not the only way to create cohesive effects. Numerous experiments studying the packing of rods, granular chains, and more complex 3D printed grains may support tensile stresses [19, 21, 47–59]. For a review of the packing and rheology of nonspherical, elongated grains, see Ref. 59.

Rods within a granular assembly lack rotational freedom, and through this frustration of motion, an effective tensile strength develops. Granular rod piles may form with wall angles of $90°$ or more because of this effective cohesion. The stability and packing of rods is sensitive to the length to diameter ratio of the rods [47, 48, 53]. Longer rods pack together in lower volume fraction ensembles [47] and can be built into taller stable ensembles [53]. Another example of a nonspherical granular system is ensembles of granular chains, solid spheres attached by flexible links. These chains form bulk materials with yield strength that depends on the chain length [60]. Longer chains entangle in the bulk, and through experiment and simulation Brown *et al.* [60] showed that the enhanced yield properties of these ensembles were due to this entanglement.

The addition of bends at the rod ends creates a u-particle. The u-particle shape is arguably the simplest particle shape that possesses concavity. We define a concave particle as a
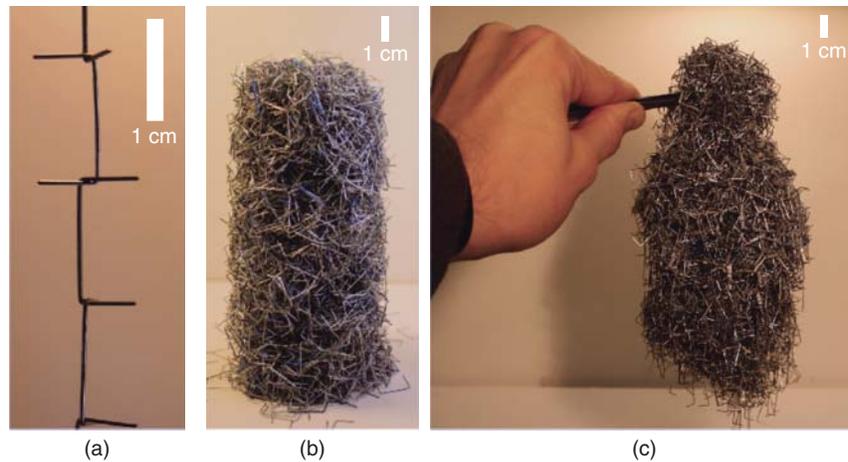
Figure 17.2 u-Particle assemblies. (a) u-Particles interpenetrate to support tensile loading. (b) A free-standing column of entangled u-particles. (c) Grasping the tower with tweezers illustrates the tensile strength of this granular assembly.

solid body where there may be found a line segment that connects two sections of the particle while not being fully contained within the solid body of the particle. For the purposes of u-particles, line segments connecting points on opposing barbs must pass through the free-space between the barbs, and thus the particle shape is concave. The concavity of a u-particle is defined as the total volume of the concave internal region of the particle. For u-particles, the concavity may be varied by changing the length of the ends compared to the width of the opening. Clusters of u-particles readily form mechanically entangled solids that are easily formed into columns that maintain their shape under gravity and, when pulled from the top by a pair of tweezers, may be lifted as almost a solid plug (see Fig. 17.2).

17.1.4 Characterize the Rheology of Granular Materials

Before we describe our experiments studying the stability and packing of mechanical entangled u-particle ensembles, we briefly review commonly employed experimental methods used to characterize the rheology and packing of granular material.

17.1.4.1 Packing Measurements Mechanically stable ensembles of spherical GM are found in a range of ϕ from random loose-pack $\phi_{\mathrm{rlp}} \approx 0.55$ to random close-pack volume fraction $\phi_{\mathrm{rcp}} \approx 0.64$. Although the packing fraction of ordered ensembles (i.e., on a lattice) may be analytically determined, the prediction of the maximum volume fraction for particles of arbitrary shape is a computationally intensive process [13]. A primary goal of packing studies is to understand how particles arrange in mechanically stable configurations. Furthermore, ϕ may be used as a measurement of the ensembles state and thus used to predict the dynamical response of GM subject to shear [61], impact [37], or intruder drag [62].

Study of the packing of granular media under mechanical [63] or air-fluidized [64] perturbation has revealed that the evolution of ϕ is dependent on the forcing parameters such as peak mechanical acceleration or air pressure. The relaxation dynamics of granular material are complex, exhibiting signatures of multiple timescales [64] or stretched exponential behavior [63]. A common feature of these experiments is that compaction of granular material, and subsequently the increase in ϕ, occurs slowly, over many thousands of iterations.

17.1.4.2 Stress–Strain Rheology Stress–strain experiments are a fundamental tool used to develop and test constitutive equations of material flow. The stress–strain response of granular material subject to a wide variety of tests in various geometries has been studied [1–4, 65]. The prototypical stress–strain experiment is simple shear in which granular material is placed between two (semi-)infinite, horizontal, planes with the top plane translated at constant velocity. An important note about stress–strain experiments is that they effectively take place in a steady-state in which the force along the moving plate fluctuates about a mean value that will persist as long as the experiment proceeds.

17.1.4.3 Vibration Experiments An important experimental tool in understanding the relaxation dynamics and steady-states of granular gases/fluids/solids results from applying uniform vibration [2, 4, 66–68]. Vibro-fluidization

has been used to study the properties of wet cohesive beads by exploring the solid–liquid and liquid–gas phase transitions that occur as a function of oscillation amplitude and frequency [45, 46, 69]. A transition from a liquid to gaseous phase occurs in wet cohesive granular media when the injected energy from vibration exceeds the capillary bond energy [69]. In avalanching experiments with dry granular media, vibration has been used to mobilize particles and thus cause the GM to relax under gravity faster or slower depending on the amplitude and frequency of vibration [68, 70]. Relaxation of slopes of granular material follows a Boltzmann-like exponential function with vibration amplitude analogous to a thermal energy [68].

17.2 EXPERIMENT

In this section, we describe a set of experiments to study the packing and relaxation of "u-particle" columns. We formed vertical, free-standing columns from collections of u-particles of varied barb length to width ratio l/w. By varying l/w, we vary the concavity of the particles with $l/w = 0$ being rods with no concave region and large l/w particles possessing a large amount of concavity. We focus on two properties of the u-particle columns: (i) the packing behavior of u-particles studied through measurement of ϕ and (ii) the relaxation of columns under gravity and subject vertical vibration from the floor (see Fig. 17.3).

17.2.1 Experimental Apparatus

U-Particles consisted of steel staples (Duo-fast; Vernon Hills, IL) of constant width, $w = 1.17$ cm, and variable barb length, l ($l/w \in [0.02, 1.125]$). The cross section of all particles was rectangular with thickness of 0.5 mm and width 1.27 mm, which corresponded to a rod-like aspect ratio for $l/w = 0.02$ particles of ≈ 14. We cut particles to size $l/w = 0.02 \pm 0.02, 0.13 \pm 0.02, 0.15 \pm 0.03,$ and 0.28 ± 0.04, and other particles were purchased at that size.

Collections of monodisperse particles with fixed l/w were formed into free standing cylindrical columns with column diameter, $d = 4.4$ cm or $d = 5.6$ cm, and height, $h_0 = 3$ cm. Columns were prepared by pouring particles into the cylindrical container followed by a 20 s sinusoidal vibration of the base at a frequency, $f = 30$ Hz, and peak acceleration, $\Gamma = 2$ (in units of gravitational acceleration g). We confirmed that steady-state volume fraction was reached through our preparation protocol in separate experiments conducted over a 60 s time period. Columns occupied a volume $V = \pi h (d/2)^2$, and the volume fraction was calculated as $\phi = \frac{M}{\rho_{st} V}$ where M is total particle mass and $\rho_{st} = 7.85$ g/cm^3 is the density of steel.

Sinusoidal oscillation was generated by an electromagnetic shaker (VTS; Aurora, OH; Fig. 17.1c). The shaker piston was attached to a linear, square-shaft, air bearing, which insured that the motion was primarily vertical. The shaker was mounted to a thick aluminum plate through a collection of springs. This mounting system reduced vibrational coupling, which would occur if the shaker was mounted to the ground. Vibration experiments were performed at a frequency of $f = 30$ Hz and variable peak acceleration $\Gamma \in [1.2, 2.5]$ (in units of gravitational acceleration g). The shaker was controlled by LabVIEW and a Tecron 7550 power amplifier. Acceleration of the vibration table was measured by an accelerometer embedded in the vibration table (PCB Piezotronics; Depew, New York).

Column collapse was monitored using a high-speed camera (Point-Grey; Richmond, BC, Canada). Image capture was triggered externally by a function generator controlled by LabVIEW such that images were captured at a
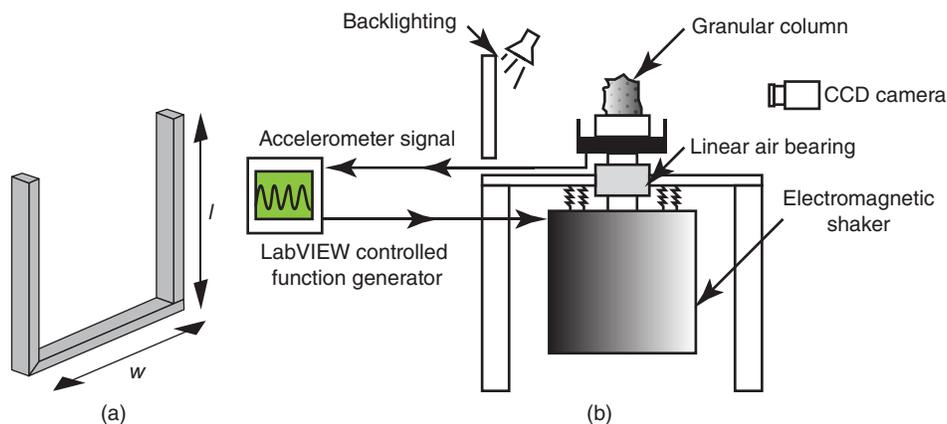
Figure 17.3 Relaxation dynamics of U-particle columns are studied through a mechanical vibration experiment. (a) U-Particle geometry. Width, w, is held constant and length, l, is varied. (b) A computer-controlled shaker table applies sinusoidal forcing to a granular column. A high-speed camera records column collapse from the side.

constant phase of the oscillation cycle, and at frequencies of f, $f/2$, and $f/4$. Images were analyzed in Matlab. Columns appeared black on a white background, and we extracted the foreground column using an image threshold. We then dilated the foreground region to insure that the column was a singly connected region and finally measured the centroid height, $h(t)$, of the column and the projected 2D area $A(t)$.

17.2.2 Packing Experiments

Particles were poured into the cylinder and came to rest at an initial volume fraction ϕ_0, which was dependent on particle packing (Fig. 17.4). Applying vibration for 60 s resulted in a steady-state final volume fraction, ϕ_f, which reached steady-state within approximately 20 s. As can be seen in Figure 17.4b, ϕ_0 and ϕ_f decreased with increasing l/w. Compaction, defined as $\chi = \frac{\phi_f - \phi_0}{\phi_0}$, linearly increased with l/w and was fit by the function $\chi = 0.23(l/w) + 0.12$ ($R^2 = 0.65$). Larger l/w particles likely exhibit a higher compaction because their long barbs cause them to jam in lower ϕ_0 initial states, while their large internal volume also allows packing to high ϕ_f.

For a comparison with similar experiments, the value of $\phi_f = 0.28 \pm 0.01$ we observed for $l/w = 0.02$ particles is close to the range $\phi_f = 0.28$–0.34, observed in cylindrical rod packs with comparable aspect ratio (length/thickness

≈ 14) [48, 52, 71, 72]. The variation in cylinder rod values was due to difference in preparation method. The lower value observed in our $l/w = 0.02$ particles is likely due to the fact that our particle have a rectangular cross section while the values we compare to are from cylindrical cross-sectional rods.

The final volume fraction, ϕ_f, decreased monotonically with increasing l/w. This is consistent with what is observed in rod packing studies in which increasing the length (aspect ratio) of rods decreases the volume fraction [48, 52, 71, 72]. For long rods, the volume fraction scales inversely with rod length, and this behavior is described through a statistical model of particle packing called the random contact model, which we describe in Section 17.3. One way to qualitatively understand this decrease in ϕ_f with increasing l/w is that larger l/w particles have larger internal volumes and thus pack less efficiently.

17.2.3 Collapse Experiments

After we formed cylinders of packed u-particles in the packing experiment, we removed the confining container; this left the column free-standing. During removal of the confining cylinder, the $l/w = 0.02$ particles were marginally stable with partial column collapse occurring approximately 50% of the time, similar to the results reported in Ref. 53. Spontaneous collapse of the $l/w > 0.02$ columns was rarely
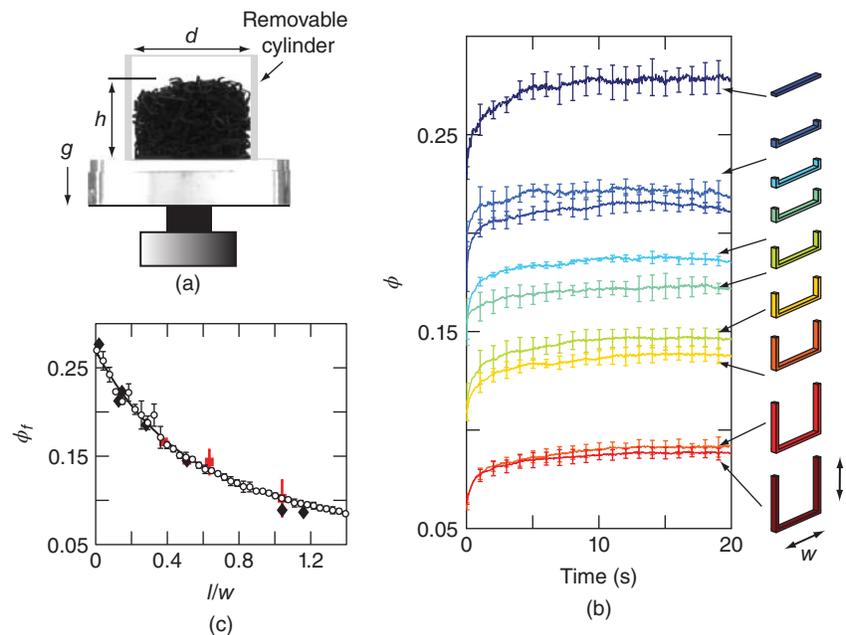
Figure 17.4 Formation and packing of u-particle columns. (a) Experimental setup to form free-standing u-particle columns. Particles were packed within a containing cylinder of diameter $d = 4.4$ cm or $d = 5.6$ cm, which was removed after the packing protocol. (b) $\phi(t)$ during column preparation for various u-particle assemblies. (c) Final packing fraction, ϕ_f, as a function of particle geometry in experiment (column diameter $d = 4.4$ cm diamonds and $d = 5.6$ cm squares) and simulation (white circles). Line is theory prediction from the random contact model.
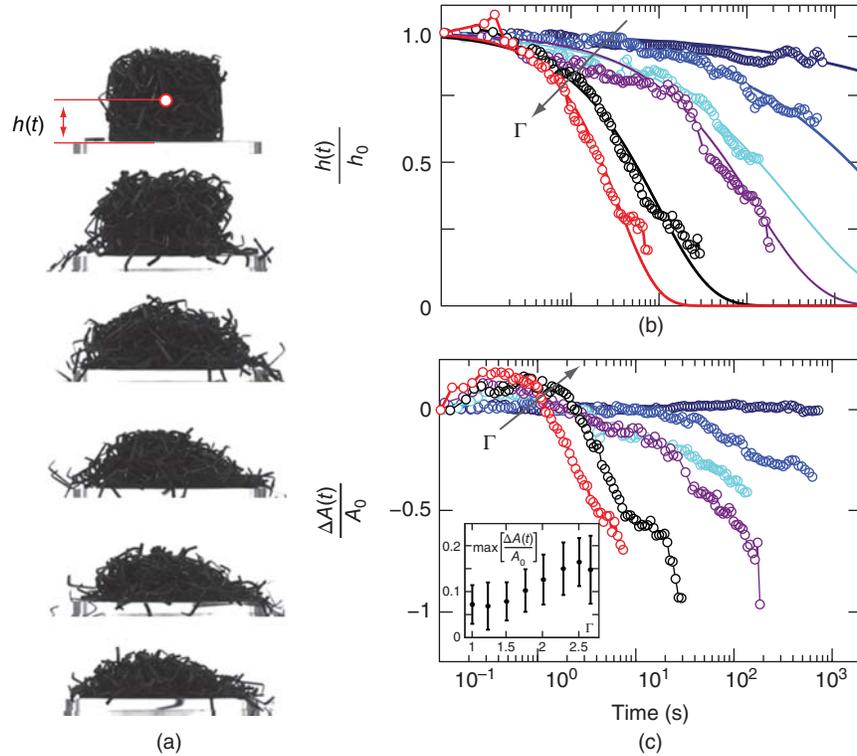
Figure 17.5 Column collapse dynamics. (a) The normalized centroid height, $h(t)/h_0$, of the column during collapse. Vibration parameters are $\Gamma = 2, f = 30$ Hz, and images are separated by 90 oscillation periods. (b) Relaxation of $h(t)/h_0$ as a function of time is shown for $l/w = 0.379$ for $\Gamma = 1.23, 1.48, 1.70, 1.96, 2.20, 2.53$, respectively (arrow denotes increasing Γ). Fit lines are stretched exponentials with equation given in the text. (c) Change in projected area of the column, $\frac{\Delta A(t)}{A_0}$, as a function of time. Γ corresponds to values in (b) with arrow denoting direction of increasing Γ. Inset shows the peak area increase, $\max[\frac{\Delta A(t)}{A_0}]$, as a function of Γ averaged over all l/w (error bars are standard deviation).

observed. To explore the dynamical stability of u-particle columns, we next subjected them to vertical vibration from the base and observed column collapse.

We applied sinusoidal vibration to the base of the free-standing column and observed the collapse process from a lateral view with our camera (Fig. 17.5a). We characterized collapse dynamics by monitoring the centroid height, $h(t)$, and cross-sectional area, $A(t)$, of the column (Fig. 17.5b). The collapse dynamics of $h(t)$ were well described by a phenomenological stretched exponential fit function $\frac{h(t)}{h_0} = e^{[-(\frac{t}{\tau})^\beta]}$. The parameter τ is the characteristic collapse time and β is the stretching parameter [73]. Consistent with previous studies [63, 74], β was in the range of 0.5–1 and decreased slightly as Γ increased but was independent of particle geometry. The stretched exponential function is frequently applied to the description of relaxation dynamics of disordered systems [73]; however, a physical interpretation of how it applies to the collapse of geometrically entangled particles is an open question.

For fixed l/w, the collapse time of the column found from the stretched exponential, τ, decreased with increasing Γ. This supports our intuition that larger perturbations cause a more rapid collapse of the column. Furthermore, the logarithm of τ increased linearly with $1/\Gamma$ (Fig. 17.4a) and τ was fit by an exponential $\tau = f^{-1}e^{\Delta/\Gamma}$ with Δ as the single fit parameter ($f = 30$ Hz).

The exponential fit is indicative of an Arrhenius-like process observed in the relaxation of activated systems. The Arrhenius process describes the escape probability of a thermally or mechanically activated particle from a potential well of depth Δ. In thermal systems, the escape time is proportional to one over the Boltzmann factor $\exp\left(-\frac{E}{kT}\right)$, where E is the activation energy required to overcome the potential barrier. In our system, thermal effects are negligible, and instead mechanical excitation plays the role of a thermal energy-like source (Γ analogous to kT) and Δ is analogous to an energy barrier resulting from particle entanglement.

The second quantity we measured during column collapse was the change in projected cross-sectional area, $\frac{\Delta A(t)}{\Delta T}$ of the column. The cross-sectional area displayed an initial increase during the first second of vibration indicating that prior to collapse and particle shedding from the column, the structure initially expands (dilates). The amount of dilation

that occurred during collapse, $\max[\frac{\Delta A(t)}{A_0}]$, was an increasing function of Γ for all experiments (see inset Fig. 17.5b).

The stretched exponential fit (Fig. 17.5) suggests that the column collapse process may be qualitatively similar across varied Γ with only the timescale changing. However, the variation in column dilation during collapse suggests that the internal particle processes leading to collapse may differ as a function of Γ. At small Γ, we hypothesize that frictional contacts are mobilized through vibration and thus particles can relax through a sliding process while collisions are not important. At higher Γ, we observe that particles appear highly mobilized and often collide with each other, which likely leads to the dilation we observe during the initial collapse process. Thus, we hypothesize that in different regimes of Γ, the particle scale dynamics of collapse may differ; however, the macroscale collapse time is well described by the stretched exponential.

Column collapse occurred through the separation of entangled particles during vibration. We therefore expected that the hindrance of motion due to particle entanglement – and thus Δ – would increase monotonically with the size of the concave region and thus particle length. Instead we found that Δ was a nonmonotonic function of l/w (Fig. 17.6) with Δ reaching a maximum value at intermediate $l/w = 0.394 \pm 0.045$.[1] Δ appears in an exponential, and, thus, the relaxation time for fixed Γ displays a strong sensitivity to the variation of particle shape (see inset Fig. 17.6). We posit that the maximum in Δ is related to the statistics of particle entanglement within the bulk, and we next study entanglement propensity in theory and simulation.
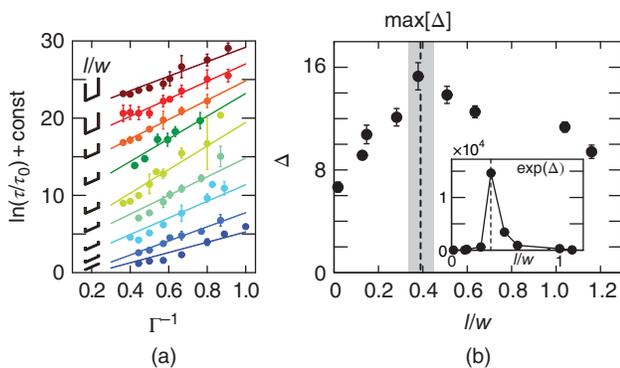
Figure 17.6 Timescale of collapse process. (a) The logarithm of the relaxation time versus inverse acceleration with exponential fit lines $\tau = f^{-1}e^{\Delta/\Gamma}$ ($\tau_0 = 1$ s). Curves are offset vertically for clarity. Error bars are standard deviation of 4 or greater replicates. (b) Δ as a function of l/w. Dashed line indicates estimated maximum of Δ (see Ref. [16]). Error bars represent 95% confidence interval of the best fit lines from (a). Source: Figure reprinted from Ref. [16].

[1]We estimate the maximum and standard deviation of l/w in experiment using a weighted average of points near the peak.

17.3 SIMULATION

In this section, we describe modeling of u-particle packing and examine the ability of particles to mechanically entangle as a function of particle shape. We discuss how excluded volume plays an important role in particle ensembles in which only steric interactions are important, such as our macroscale granular particles. We introduce the random contact model proposed for colloidal rods. We apply this model to our u-particle system and obtain good agreement between the model and our experimental results. Finally, we generate u-particle ensembles in computer simulation and investigate the statistical packing properties of particle arrangements. We show that particles at intermediate l/w display maximum particle entanglement. Lastly, we discuss the relationship between the non-monotonic particle entanglement statistics from simulation, and the non-monotonic relaxation dynamics of columns as measured in experiment.

17.3.1 Random Contact Model of Rods

The random contact model was originally proposed to describe the packing of straight, rod-shaped colloids [72]. This model relates the bulk volume fraction, ϕ, of the ensemble to the particle volume, V_p, and excluded volume, V_e, of the constituent particles. The random contact model assumes only that particles are homogeneously distributed in space and has been shown to work well for rod-shaped particles over a large range of aspect ratios [48, 71, 72, 72]. In the following, we derive the random contact model and explain how it is used in the calculation of "u-particle" packing statistics.

The particle's excluded volume is defined as the volume of space that one particle excludes from another, averaged over all possible particle–particle configurations. Another definition of V_e is in relation to the probability of finding two particles in contact within a larger volume, V. This can be represented as

$$V_e = pV, \qquad (17.1)$$

where p is the contact probability. A simple example to consider is a spherical particle of radius r. A spherical particle excludes a volume $V_e = \frac{4}{3}\pi(2r)^3$ from another identical particle. Thus, there is a volume of space, V_e, in which particles cannot be placed without overlapping the original particle. This again is indicative of the probabilistic nature of excluded volume since the probability to randomly place a sphere in a position overlapping the original sphere is $p = \frac{V_e}{V}$.

The relationship between volume fraction and V_e can be determined by the following method. For a volume of space, V with N particles of volume V_p, the solid volume occupied by the particles is $V_o = NV_p$. The volume fraction is defined as $\phi = \frac{V_o}{V}$, which using Equation 17.1 we can rewrite
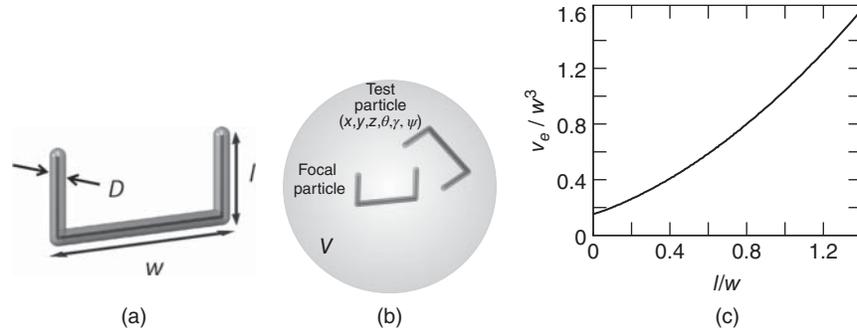
Figure 17.7 Overview of simulation. (a) Three spherocylinders form a u-particle in computer simulation with dimensions given in the text. (b) We compute the excluded volume of u-particles through a Monte Carlo simulation measuring the probability for two randomly placed particles to overlap within a large volume V. (c) Excluded volume of u-particles as a function of l/w.

as $\phi = pN\frac{V_p}{V_e}$. We interpret pN as the average number of contacts per particle within the packing, C, and arrive at the random contact equation[2]

$$\phi = C\frac{V_p}{V_e}. \tag{17.2}$$

The random contact model describes the bulk packing of homogeneously distributed particles in free space, with particle properties V_p and V_e and average contact number C. This model has been tested in experiment and simulation with rod-shaped objects at the microscopic and macroscopic scales [48, 52, 71, 72], and surprisingly all experiments have found a similar contact number $C \approx 10$. We note that this model is applicable for particles that pack with spatially uncorrelated contact points. Applying this model to spheres fails because contact points between particles are always spatially correlated (by definition a distance from particle location).

We compute V_e numerically for u-particles in a Monte Carlo simulation by using the probabilistic definition of excluded volume. We form u-particles from a combination of three spherocylinders oriented at right angles with each other to form a u-particle. u-Particle dimensions are normalized by the spherocylinder cross-sectional diameter, D. The width of the base spherocylinder is fixed at 14D and the barb lengths are varied from 0 to 16D, consistent with the u-particles used in experiment. In simulation, we randomly place test-particles within a large volume, V, with respect to a focal particle fixed at the center. For each iteration of the computation, we choose a random location (x, y, z) and random orientation (defined by the Euler angles

of the particle, θ, γ, ψ) to place the test particle. We then check if the test particle overlaps with the focal particle at this location–orientation combination. To determine the overlap of two u-particles, we must simply compute the pairwise minimum distance between each particle's constituent spherocylinders. If any of these nine pairwise distances are less than the spherocylinder diameter, D, the particles overlap. To detect if particles overlap, we compute the minimum distance between two line segments along the centers of the spherocylinders. We compute the distance between line segments using an algorithm originally developed for computer graphics [75].[3] If particles are found to overlap, we increment a counter N_o. After N iterations of this algorithm, the fraction $\frac{N_c}{N} \to p$ and thus our calculation converges on the excluded volume $V_e = V\frac{N_c}{N}$.

We fit a polynomial to V_e and find that $V_e = 0.460(l/w)^2 + 0.530(l/w) + 0.148$ (in units of W^3, see Fig. 17.7). We approximate the particle volume as $V_p = \pi W(D/2)^2 + 2\pi L(D/2)^2 + \frac{4}{3}\pi(D/2)^3$. With a contact number $C = 9$, the measured volume fraction in experiments and the random contact model prediction are in a good agreement. This value of C is close to the values reported for rod packings of $C = 8.4$–10.8, which depends on preparation [47, 48, 71]; this is surprising given the difference in particle shape between rods and u-particles. We emphasize that the random contact model may only be applied to particles in which the spatial arrangement of contacts is suitably random (i.e., cannot be used for spheres). This process does not work for sphere or for near-sphere packings, which have a lower contact number [76]. Having verified that the random contact model works for u-particles, we may proceed with the calculation of packing statistics for u-particle ensembles.

---

[2]We note that in the original text of Philipse [72], the random contact model is introduced with the prefactor $2\langle c \rangle$ instead of C. In this case, $\langle c \rangle$ is the ratio of total number of contacts by the number of particles and multiplying this value by two results in, C the average number of contacts per particle. We use this form of the equation in the text and when comparing to studies using the alternate version, we convert reported values of $\langle c \rangle$ to C.

[3]We have uploaded a Matlab implementation of this algorithm to http://www.mathworks.com/matlabcentral/fileexchange/32487-shortest-distance-between-two-line-segments.

17.3.2 Packing Simulations

We study the packing of u-particles in a computer simulation to identify properties of the particle entanglement within the pile. Particle packings were generated through a Monte Carlo simulation. We do not perform molecular dynamics in these simulations; instead we solely enforce the condition that particle configurations which result in an overlap are not allowed. From these packings, we study the statistics of u-particle entanglement.

To generate u-particle packings, we used a brute force packing algorithm to generate close packings of nonoverlapping particles. Packing proceeded in two steps: In the first step, particles were placed at random position and orientation inside a cubic volume of cross-sectional area $(52 \times 52 D^2)$ such that the particles did not overlap. If a newly placed particle resulted in an overlap, this particle was removed and a new position was randomly selected. If after 10,000 iterations a suitable particle location was not found, then the algorithm proceeded to step two. In the second step, particles in the volume were selected at random and displaced downward a small random direction and distance $\frac{D}{10}$. If the new location of the particle resulted in particle overlap, the particle was returned to the original location and a new particle chosen. The algorithm was halted after the center of mass height of the ensemble appeared to reach a steady-state. The volume fraction of the simulated packings was determined by measuring the average height of the pile and multiplying it by the areal dimension to obtain the occupied volume and then dividing this by the total volume of particles. A sample packing simulation and packing dynamics are shown in Figure 17.8. In simulation, particles gradually approach a steady-state volume fraction that is consistent with the experimental data (Fig. 17.4c).

We hypothesized that particle entanglement within the column would influence the relaxation time during vertical vibration. Thus, we expected that the maximum in Δ should correspond to a maximum in the density of particle entanglements. In simulation, we defined two particles as entangled when the center line of one particle intersected the internal plane of the neighboring particle (see inset Fig. 17.5a). We measured the number of entanglements per particle, N, for each particle in simulation. The probability distribution function, $P(N)$, was sensitive to l/w (Fig. 17.5a) with mean value $\langle N \rangle$ increasing monotonically with l/w (Fig. 17.5b). The increase was sublinear, indicating that $\langle N \rangle$ grew slower than that of the particle's convex area $(l - D)(w - 2D)$.

The scaling of $\langle N \rangle$ with l/w can be determined by considering the solid volume occupied by the entangled particles in the focal particles convex region (the convex area with infinitesimal thickness δ). Assuming a homogeneous packing, the solid volume in this region is $V_{\text{ent}} = \phi_f (l - D)(w - 2D) \delta$. Since each entangled particle contributes only a portion to V_{ent} in the shape of an ellipse of thickness δ, on average $V_{\text{ent}} = \alpha \langle N \rangle \pi \delta \frac{D^2}{4}$ where $\alpha > 1$ accounts for the nonplanar crossings (Fig. 17.9). Solving the above relations yields

$$\langle N \rangle = \frac{4C}{\alpha} \left(\frac{V_p(l - D)(w - 2D)}{\pi V_e D^2} \right). \tag{17.3}$$

With a single fit parameter, $\alpha = 2.648 \pm 0.108$, we find excellent agreement between the predicted number of entanglements per particle and those measured in simulation (Fig. 17.10b).

The spatial density of particle entanglements is $\rho_{\text{ent}} = \langle N \rangle \rho$ where $\rho = \frac{C}{V_e}$ is the number density of particles (Fig. 17.10b). Substitution for $\langle N \rangle$ yields

$$\rho_{\text{ent}} = \frac{4C^2}{\pi \alpha} \left(\frac{V_p(l - D)(w - 2D)}{V_e^2 D^2} \right) \tag{17.4}$$

(a)   (b)
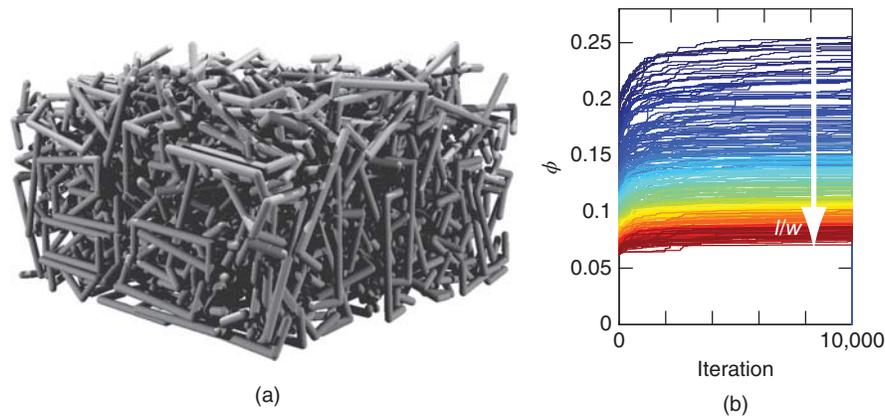
Figure 17.8 Computer simulated u-particle ensembles. (a) A computer-generated ensemble of u-particles of $l/w = 0.35$. (b) Volume fraction of particle ensembles as a function of simulation iteration. Particle ensembles are packed together in a Monte Carlo simulation until the volume fraction reaches a steady-state. Particle l/w is varied from 0 to 1.4 with increasing l/w indicated by arrow.
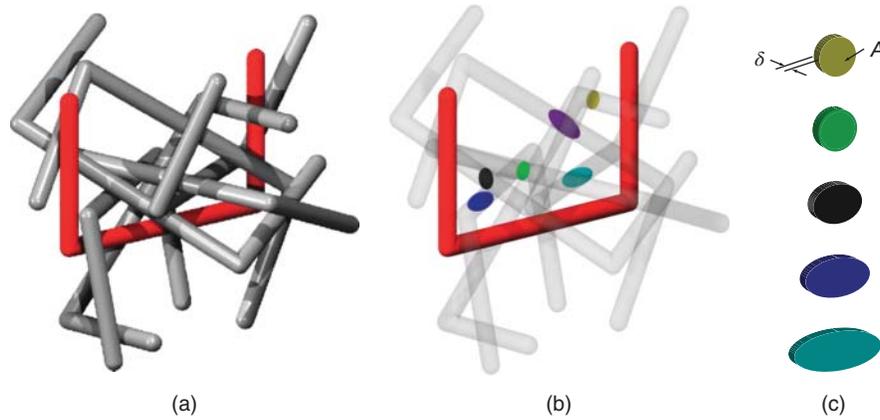
Figure 17.9 Entanglement counting in simulation. (a) A rendering of entangled particles within the ensemble. (b) To predict the number of entanglements within the packing, we consider the infinitesimally thin volume of space within the concave region of the central focal particle (dark gray). The intersection of entangled particles with this plane forms thin ellipses. (c) The cross-sectional area of the intersection region can vary from a circle of diameter D to an ellipse with minor axis $D/2$.
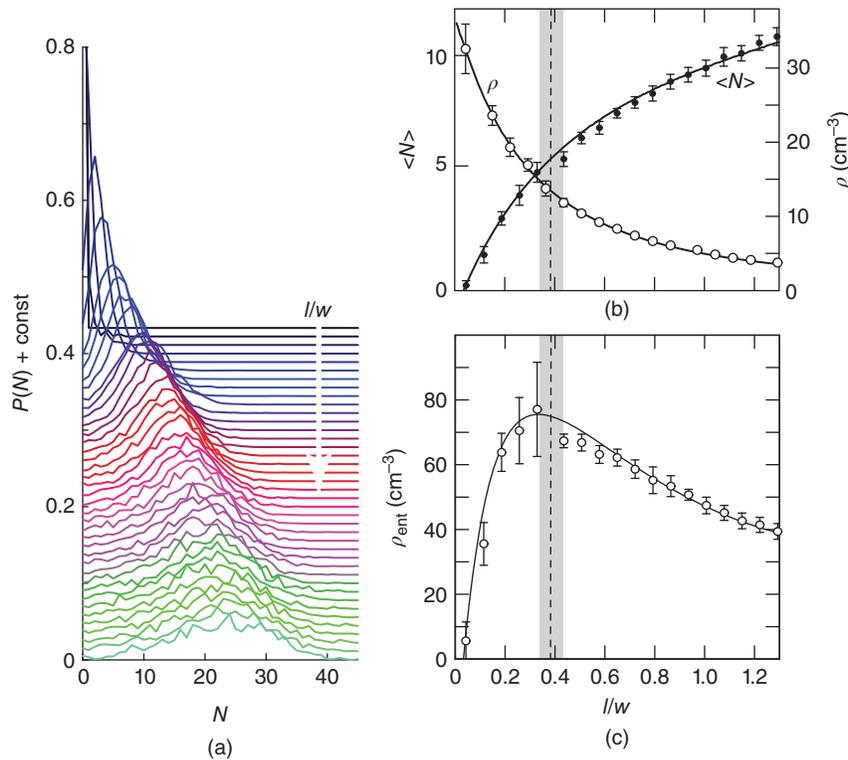
Figure 17.10 Statistics of particle entanglement in simulation. (a) The probability distribution of entanglement number, N, as a function of l/w. Curves are shifted vertically for clarity; $l/w = 0$ at top and increases in increments of 0.036 down. (b) Mean values for N and ρ measured in simulation (circles) and the theoretical fit (black line). (c) Density of entanglements as a function of l/w and the theoretical fit (black line). Vertical dashed line and gray bar correspond to the mean and standard deviation of the estimated maximum of Δ from experiment. Source: Figure reprinted from Ref. [16].

and again the simulation and theory are in a good agreement (Fig. 17.10c) using the previously determined fit parameters C and α. Furthermore, the experimental maximum max[Δ] at $l/w = 0.394 \pm 0.045$ is close to the value obtained in simulation and theory of $l/w = 0.340 \pm 0.015$, suggesting that the large relaxation times for the intermediate u-particle columns are due to the large density of mechanical entanglements.

17.4 CONCLUSIONS

Similar to rod-like particles [48, 52, 71, 72], columns formed from u-particles are stabilized through the inhibition of particle rotation and translation among the entangled particles. The addition of the transverse ends, which form concave u-particles, leads to mechanical entanglement and increases column stability. However, the increase in entanglement with increasing length is offset by the decrease in particle-packing density. These two trends conspire to generate a maximum in the density of mechanical entanglements in collections of nonconvex particles of intermediate l/w—thus columns of these particles most strongly resist separation.

Relaxation processes studied under oscillatory perturbations are found in many soft-matter systems such as oscillatory shear experiments in colloids and suspensions. Vibro-fluidization has been previously used to study the relaxation of piles and columns of dry granular materials under gravity [68, 70, 77]; however, this method has not been applied to characterizing the strength of cohesive GM. We envision that vibration–relaxation experiments similar to those reported here will be useful to explore rheological properties of fluid or electrostatic mediated cohesive GM. Although granular materials in the natural world often posses some interstitial fluids, there is still much to be learned about cohesive granular materials.

Macroscale model systems similar to those described here and elsewhere [60, 78] are useful tools within which to explore how particle shape influences ensemble rheology at other scales. Future study of the particle-scale dynamics of nonconvex particles may provide further insight into the rheology of entangled or crowded particulate systems. For example, model systems such as granular particles may help understand the particle scale dynamics of anomalous diffusion within the crowded cellular environment [79–82]. Furthermore, particles found in nature are often nonspherical [14]; thus, we hope that experiments like those described here will advance the experimental and computational tools used to study nonspherical or even nonconvex particulate systems.

The random contact model utilized to explain the optimum geometry for entanglement of U-shaped particles assumes only uncorrelated particle contacts within the bulk. Thus, we expect the results to apply to rigid nonconvex particulate systems of all scales. A recent study of suspension rheology found that convex particles of differing shape collapsed to a viscosity–stress master curve while concave particle did not collapse to this curve; this difference was attributed to particle entanglement effects [17]. At the microscale, polymers with rigid pendants oriented perpendicular to the polymer chain increase internal molecular free volume and hinder polymer motion, which significantly affects rheology similar to geometric entanglement [83].

At the macroscale, strain-stiffening of model polymers is associated with entanglement [60]. Even organisms can benefit from geometric entanglement. For example, the fire ant *Solenopsis invicta* and the army ant *Eciton burchelli* create waterproof rafts and shelters—which have been described as akin to living chain mail [84]—through the interlocking and entanglement of limbs and mandibles [28, 30].

ACKNOWLEDGMENTS

REFERENCES

[1] Jaeger HM, Nagel SR. Physics of the granular state. Science 1992;255:1523–1531.

[2] Jaeger HM, Nagel SR, Behringer RP. Granular solids, liquids, and gases. Rev Mod Phys 1996;68(4):1259–1273.

[3] Nedderman RM. *Statics and Kinematics of Granular Materials*. Cambridge: Cambridge University Press; 1992.

[4] Duran J. *Sands, Powders, and Grains: An Introduction to the Physics of Granular Materials*. New York: Springer-Verlag; 2000.

[5] Liu AJ, Nagel SR. *Jamming and Rheology: Constrained Dynamics on Microscopic and Macroscopic Scales*. Boca Raton, FL: CRC Press; 2001.

[6] Cundall PA, Strack ODL. A discrete numerical model for granular assemblies. Geotechnique 1979;29:47.

[7] Silbert LE, Ertas D, Grest GS, Halsey TC, Levine D. Geometry of frictionless and frictional sphere packings. Phys Rev E 2002;65:031304.

[8] Silbert LE, Ertas D, Grest GS, Halsey TC, Levine D, Plimpton SJ. Granular flow down an inclined plane: Bagnold scaling and rheology. Phys Rev E 2001;64:051302.

[9] Silbert LE, Ertas D, Grest GS, Halsey TC, Levine D. Analogies between granular jamming and the liquid-glass transition. Phys Rev E 2002;65:051307.

[10] Ertas D, Grest GS, Halsey TC, Levine D, Silbert LE. Gravity-driven dense granular flows. Europhys Lett 2001;56:214.

[11] Pournin L, Weber M, Tsukahara M, Ferrez JA, Ramaioli M, Libling ThM. Three-dimensional distinct element simulation of spherocylinder crystallization. Granular Matter 2005;7:119.

[12] Azéma E, Estrada N, Radjaï F. Nonlinear effects of particle shape angularity in sheared granular media. Phys Rev E 2012;86:041301.

[13] Damasceno PF, Engel M, Glotzer SC. Predictive self-assembly of polyhedra into complex structures. Science 2012;337(6093):453–457.

[14] Cho GC, Dodds J, Santamarina JC. Particle shape effects on packing density, stiffness, and strength: natural and crushed sands. J Geotech Geoenviron Eng 2006;132(5):591–602.

[15] Meng L, Li S, Lu P, Li T, Jin W. Bending and elongation effects on the random packing of curved spherocylinders. Phys Rev E 2012;86(6):061309.

[16] Gravish N, Franklin SV, Hu DL, Goldman DI. Entangled granular media. Phys Rev Lett 2012;108(20):208001.

[17] Brown E, Zhang H, Forman NA, Maynor BW, Betts DE, DeSimone JM, Jaeger HM. Shear thickening and jamming in densely packed suspensions of different particle shapes. Phys Rev E 2011;84:031408.

[18] Baule A, Makse HA. Fundamental challenges in packing problems: from spherical to non-spherical particles. Soft Matter 2014;10(25):4423.

[19] Miskin MZ, Jaeger HM. Adapting granular materials through artificial evolution. Nat Mater 2013;12(4):326–331.

[20] Brown E, Rodenberg N, Amend J, Mozeika A, Steltz E, Zakin MR, Lipson H, Jaeger HM. Universal robotic gripper based on the jamming of granular material. Proc Natl Acad Sci U S A 2010;107(44):18809–18814.

[21] Stannarius R. Granular materials of anisometric grains. Soft Matter 2013;9(31):7401.

[22] Manna L, Milliron DJ, Meisel A, Scher EC, Alivisatos AP. Controlled growth of tetrapod-branched inorganic nanocrystals. Nat Mater 2003;2(6):382–385.

[23] Glotzer SC, Solomon MJ. Anisotropy of building blocks and their assembly into complex structures. Nat Mater 2007;6(8):557–562.

[24] McKeown NB, Budd PM. Exploitation of intrinsic microporosity in polymer-based materials. Macromolecules 2010;43(12):5163–5176.

[25] McKeown NB, Budd PM, Msayib KJ, Ghanem BS, Kingston HJ, Tattershall CE, Makhseed S, Reynolds KJ, Fritsch D. Polymers of intrinsic microporosity (PIMS): bridging the void between microporous and polymeric materials. Chem Eur J 2005;11(9):2610–2620.

[26] Whitesides GM, Boncheva M. Beyond molecules: self-assembly of mesoscopic and macroscopic components. Proc Natl Acad Sci U S A 2002;99(8):4769–4774.

[27] Miao L, Vanderlinde O, Liu J, Grant RP, Wouterse A, Shimabukuro K, Philipse A, Stewart M, Roberts TM. The role of filament-packing dynamics in powering amoeboid cell motility. Proc Natl Acad Sci U S A 2008;105(14):5390–5395.

[28] Mlot NJ, Tovey CA, Hu DL. Fire ants self-assemble into waterproof rafts to survive floods. Proc Natl Acad Sci U S A 2011;108(19):7669–7673.

[29] Franks NR. Thermoregulation in army ant bivouacs. Physiol Entomol 2008;14(4):397–404.

[30] Anderson C, Theraulaz G, Deneubourg J-L. Self-assemblages in insect societies. Insectes Soc 2002;49(2):99–110.

[31] Elliott JM, Hansell MH. Animal architecture and building behaviour. J Anim Ecol 1984;54(2):676.

[32] Chen S, Wang ZL, Ballato J, Foulger SH, Carroll DL. Monopod, bipod, tripod, and tetrapod gold nanocrystals. J Am Chem Soc 2003;125(52):16186–16187.

[33] de Gennes P-G. Granular matter: a tentative view. Rev Mod Phys 1999;71(2):374–382.

[34] Jerkins M, Schröter M, Swinney HL, Senden TJ, Saadatfar M, Aste T. Onset of mechanical stability in random packings of frictional spheres. Phys Rev Lett 2008;101:018301.

[35] Cates ME, Wittmer JP, Bouchaud JP, Claudin P. Jamming, force chains, and fragile matter. Phys Rev Lett 1998;81(9):1841–1844.

[36] Majmudar TS, Behringer RP. Contact force measurements and stress-induced anisotropy in granular materials. Nature 2005;435(7045):1079–1082.

[37] Umbanhowar P, Goldman DI. Granular impact and the critical packing state. Phys Rev E 2010;82(1):010301.

[38] Mitarai N, Nori F. Wet granular materials. Adv Phys 2006;55(1–2):1–45.

[39] Herminghaus S. Dynamics of wet granular matter. Adv Phys 2005;54(3):221–261.

[40] Richefeu V, Radjaı F, El Youssoufi MS. Stress transmission in wet granular materials. Eur Phys J E 2006;21(4):359–369.

[41] Richefeu V, El Youssoufi MS, Radjaï F. Shear strength properties of wet granular materials. Phys Rev E 2006;73(5):051304.

[42] Nowak S, Samadani A, Kudrolli A. Maximum angle of stability of a wet granular pile. Nat Phys 2005;1(1):50–52.

[43] Tegzes P, Vicsek T, Schiffer P. Avalanche dynamics in wet granular materials. Phys Rev Lett 2002;89(9):94301.

[44] Fournier Z, Geromichalos D, Herminghaus S, Kohonen MM, Mugele F, Scheel M, Schulz M, Schulz B, Schier Ch, Seemann R, Skudelny A. Mechanical properties of wet granular materials. J Phys Condens Matter 2005;17(9):S477.

[45] Scheel M, Geromichalos D, Herminghaus S. Wet granular matter under vertical agitation. J Phys Condens Matter 2004;16(38):S4213.

[46] Fingerle A, Roeller K, Huang K, Herminghaus S. Phase transitions far from equilibrium in wet granular matter. New J Phys 2008;10(5):053020.

[47] Philipse AP. The random contact equation and its implications for (colloidal) rods in packings, suspensions, and anisotropic powders. Langmuir 1996;12:1127.

[48] Blouwolff J, Fraden S. The coordination number of granular cylinders. Europhys Lett 2006;76:1095.

[49] Lumay G, Vandewalle N. Compaction of anisotropic granular materials: experiments and simulations. Phys Rev E 2004;70:051314.

[50] Galanis J, Harries D, Sackett DL, Losert W, Nossal R. Spontaneous patterning of confined granular rods. Phys Rev Lett 2006;96(2):028002.

[51] Stokely K, Diacou A, Franklin SV. Two-dimensional packing in prolate granular materials. Phys Rev E 2003;67(5):051302.

[52] Desmond K, Franklin SV. Jamming of three-dimensional prolate granular materials. Phys Rev E 2006;73(3):031306.

[53] Trepanier M, Franklin SV. Column collapse of granular rods. Phys Rev E 2010;82(1):011308.

[54] Saraf S, Franklin SV. Power-law flow statistics in anisometric (wedge) hoppers. Physical Review E 2011;83(3):030301.

[55] Zou L-N, Cheng X, Rivers ML, Jaeger HM, Nagel SR. The packing of granular polymer chains. Science 2009;326(5951):408–410.

[56] Karayiannis NCh, Foteinopoulou K, Laso M. Contact network in nearly jammed disordered packings of hard-sphere chains. Phys Rev E 2009;80(1):011307.

[57] Lopatina LM, Reichhardt CJO, Reichhardt C. Jamming in granular polymers. Phys Rev E 2011;84(1):011303.

[58] Mohaddespour A, Hill RJ. Granular polymer composites. Soft Matter 2012;8(48):12060–12065.

[59] Borzsonyi T, Stannarius R. Granular materials composed of shape-anisotropic grains. Soft Matter 2013;9: 7401–7418.

[60] Brown E, Nasto A, Athanassiadis AG, Jaeger HM. Strain stiffening in random packings of entangled granular chains. Phys Rev Lett 2012;108(10):108302.

[61] Schofield AN, Wroth P. *Critical State Soil Mechanics*. New York: McGraw-Hill; 1968.

[62] Gravish N, Umbanhowar PB, Goldman DI. Force and flow transition in plowed granular media. Phys Rev Lett 2010;105(12):128301.

[63] Philippe P, Bideau D. Compaction dynamics of a granular medium under vertical tapping. Europhys Lett 2007;60(5):677.

[64] Knight JB, Fandrich CG, Lau CN, Jaeger HM, Nagel SR. Density relaxation in a vibrated granular material. Phys Rev E 1995;51(5):3957.

[65] Oda M, Kazama H. Microstructure of shear bands and its relation to the mechanisms of dilatancy and failure of dense granular soils. Geotechnique 1998;48(4):465–481.

[66] Knight JB, Jaeger HM, Nagel SR. Vibration-induced size separation in granular media: the convection connection. Phys Rev Lett 1993;70(24):3728–3731.

[67] De Bruyn JR, Bizon C, Shattuck MD, Goldman D, Swift JB, Swinney HL. Continuum-type stability balloon in oscillated granular layers. Phys Rev Lett 1998;81(7):1421–1424.

[68] Jaeger HM, Liu C-H, Nagel SR. Relaxation at the angle of repose. Phys Rev Lett 1989;62(1):40–43.

[69] Huang K, Röller K, Herminghaus S. Universal and non-universal aspects of wet granular matter under vertical vibrations. Eur Phys J Spec Top 2009;179(1):25–32.

[70] Rubin D, Goldenson N, Voth GA. Failure and strengthening of granular slopes under horizontal vibration. Phys Rev E 2006;74(5):051307.

[71] Wouterse A, Luding S, Philipse AP. On contact numbers in random rod packings. Granular Matter 2009;11(3):169–177.

[72] Philipse AP. The random contact equation and its implications for (colloidal) rods in packings, suspensions, and anisotropic powders. Langmuir 1996;12(5):1127–1133.

[73] Phillips JC. Stretched exponential relaxation in molecular and electronic glasses. Rep Prog Phys 1999;59(9):1133.

[74] Mattsson J, Wyss HM, Fernandez-Nieves A, Miyazaki K, Hu Z, Reichman DR, Weitz DA. Soft colloids make strong glasses. Nature 2009;462(7269):83–86.

[75] Eberly DH. *3D Game Engine Design: A Practical Approach to Real-Time Computer Graphics*. San Francisco (CA): Morgan Kaufmann Publishers; 2007.

[76] Donev A, Cisse I, Sachs D, Variano EA, Stillinger FH, Connelly R, Torquato S, Chaikin PM. Improving the density of jammed disordered packings using ellipsoids. Science 2004;303(5660):990–993.

[77] Sánchez I, Raynaud F, Lanuza J, Andreotti B, Clément E, Aranson IS. Spreading of a granular droplet. Phys Rev E 2007;76(6):060301.

[78] Raymer DM, Smith DE. Spontaneous knotting of an agitated string. Proc Natl Acad Sci U S A 2007;104(42):16432–16437.

[79] Wong IY, Gardel ML, Reichman DR, Weeks ER, Valentine MT, Bausch AR, Weitz DA. Anomalous diffusion probes microstructure dynamics of entangled F-actin networks. Phys Rev Lett 2004;92(17):178101.

[80] Szymanski J, Weiss M. Elucidating the origin of anomalous diffusion in crowded fluids. Phys Rev Lett 2009;103:038102.

[81] Saxton MJ. Anomalous diffusion due to obstacles: a Monte Carlo study. Biophys J 1994;66(2):394–401.

[82] Tolić Nørrelykke IM, Munteanu E-L, Thon G, Oddershede L, Berg-Sørensen K. Anomalous diffusion in living yeast cells. Phys Rev Lett 2004;93:078102.

[83] Tsui NT, Paraskos AJ, Torun L, Swager TM, Thomas EL. Minimization of internal molecular free volume: a mechanism for the simultaneous enhancement of polymer stiffness, strength, and ductility. Macromolecules 2006;39(9):3350–3358.

[84] Mitchell M. *Complexity: A Guided Tour*. New York: Oxford University Press; 2009.